Derivation and Evaluation of a New Extinction Coefficient for use with the n-HUT Snow Emission Model

William Maslanka, Melody Sandells, Robert Gurney, Juha Lemmetyinen, Lenna Leppänen, Anna Kontu, Magret Matzl, Nick Rutter, Tom Watts, and Richard Kelly

***Abstract*— In this study, snow slab data collected from the Arctic Snow Microstructure Experiment was used in conjunction with a six-directional flux coefficient model to calculate individual slab absorption and scattering coefficients. These coefficients formed the basis for a new semi-empirical extinction coefficient model, using both frequency and optical diameter as input parameters, along with the complex dielectric constant of snow. Radiometric observations, at 18.7, 21.0, and 36.5 GHz at both horizontal and vertical polarizations, and snowpit data collected as part of the Sodankylä Radiometer Experiment were used to compare and contrast the simulated brightness temperatures produced by the n-HUT snow emission model, utilizing both the original empirical model and the new semi-empirical extinction coefficient model described here. The results show that the vertical polarization RMSE and bias values decreased when using the semi-empirical extinction coefficient; however, the horizontal polarization RMSE and bias values increased on two of the lower microwave bands tested. The unbiased RMSE was shown to decrease across all frequencies and polarizations when using the semi-empirical extinction coefficient.**

***Index Terms*—Extinction Coefficient Modelling, HUT Snow Emission Model, Microwave Scattering, Remote Sensing, Snow Emission Model.**

I. Introduction

SNOW is a vitally important variable in numerous meteorological and climatological processes, because of its high albedo, thermal emissivity, and thermal insulating properties ([1]). In addition to this, over one billion people rely on glacier and snow melt for their freshwater drinking supply ([2]), making estimations of snow mass vital for hydrological forecasts. To monitor the global snow water equivalent (SWE), passive microwave remote sensing methods have been utilized over the last 30 years ([3]–[6]) due to the all-weather capability and illumination independence that is offered by passive microwave remote sensing techniques ([7]–[9]). Passive microwave remote sensing is a viable method of global snow mass monitoring, due to the interactions between upwelling microwave radiation and snow crystals.

Observed microwave radiation of the snowpack is comprised of two contributions; from the underlying surface, and from the snowpack itself. An additional atmospheric contribution must be considered when using spaceborne sensors ([9]). Snow crystals within the snowpack act as scattering centres for the upwelling microwave radiation, meaning that the microwave signature of the snowpack is highly sensitive to the snow crystal size, the snow mass, and the radiation wavelength (and therefore its frequency, [3] and [10]).

Recently, semi-empirical models such as the n-HUT snow emission model ([11], [12]) have been used in conjunction with passive microwave remote sensing data in order to extract snow information from satellite observations ([13]). The n- HUT snow emission model is based on radiative transfer theory, treating the snowpack as a series of homogeneous layers. The basic assumption of the n-HUT model is that scattering is mostly concentrated in the forward direction, with the fraction of scattered radiation being empirically set to 0.96 ([11]). The original HUT model neglects backward scattered radiation in the radiative transfer function. It has been shown that for deep snowpacks, this may lead to increasing underestimation of brightness temperature with the HUT model, when compared to a more complete two-directional flux treatment of microwave propagation ([14]). The absorption coefficient is calculated from the complex dielectric constant of dry snow, determined from the formulae given by [15] and [16]. The extinction properties of dry snow was originally calculated as a function of both frequency and grain size, as shown by [10].

For manual characterisation of snowpack parameters, observers often describe the microstructure of the individual layers by the grain size of its ice particles, *E*, defined as ``the size of the average grains", where the size of the grains is ``its greatest extension measured in millimetres" ([17]). The conventional method for observing the grain size of a snow pack layer is done; by placing a sample of snow grains onto a millimetre grid, and visually estimating the grain size either through the use of a pocket microscope or through macrophotography and image processing ([18]). Advanced methods for quantifying the three-dimensional size of the individual snow grains have also been implemented ([19]).

Observations of grain size in the field are subject to numerous different sources of error. The preparation of the snow grains upon the millimetre grid introduces a random error

to the observation through the arbitrary selection of grains for the sample, while the measurement technique introduces the potential for observer-related errors, discussed by [20]. Three individual observers analysed macro-photographs relating to a single snow pack profile of grain size. [20] showed that an observer-related error of at least 0.25 mm was present, with samples of larger grains producing larger observer-related errors.

The Specific Surface Area (SSA) is a separate microstructure parameter that has been under increased focus over the past decade ([21]). SSA is defined as the total area at the ice/air interface per unit mass ([22]) or as the total area at the ice/air interface per unit volume ([23]), and can be observed for a snow pack via numerous different techniques; observed in the field using integrating sphere reflectance measurements (such as DUFISSS (Dual Frequency Integrating Sphere for Snow SSA measurement), [24], IceCube, [25], and IRIS, [23]), penetrometry measurements [26]–[28]), gas adsorption techniques ([22]), and computer tomography analysis ([29], [30]). SSA is inversely proportional to the optical diameter, D_o; defined as the diameter of a sphere with that shares the same SSA to that of the snow in question, regardless of the shape of the grains, and is calculated by:

$$D_o = \frac{6}{\rho_{ice} SSA} \quad (1)$$

Where SSA is measured in $m^2 \cdot kg^{-1}$, ρ_{ice} = 917 $kg \cdot m^{-3}$. Unlike grain size, which is subject to observer-related errors, D_o is a well-defined variable that can be calculated directly from observations of SSA through (1).

This paper uses the data collected as part of the Arctic Snow Microstructure Experiment (ASMEx, [31], [32]) to derive a new semi-empirical extinction coefficient for snow, using optical diameter rather than grain size as an input parameter, for use within the n-HUT model. This approach is novel, as a Flux Coefficient Model has been utilized to produce an extinction coefficient model for use within the n-HUT model using optical diameter (derived from measurements of SSA) as a direct input, rather than traditional grain size. Section II details the ASMEx campaign, and briefly describes the data collected. Section III details the Flux Coefficient Model, in which the absorption and scattering coefficients are calculated from the ASMEx data. Section IV shows the derivation of the semi-empirical extinction model, with its implementation and evaluation being shown in Section V.

II. Arctic Snow Microstructure Experiment

To derive a new semi-empirical extinction coefficient model, the radiometric and snow characteristic data of the Arctic Snow Microstructure Experiment (ASMEx, [31], [32]) were used. The radiometric observations included observations of extracted snow slabs of approximately 80 x 80 x 15 cm, extracted from naturally accumulated taiga snow, upon two bases with different radiometric properties; a reflective metal plate (a near-perfect reflector, interface reflectivity = 1), and an absorptive blackbody base (a near-perfect absorber, interface reflectivity = 0), similar to those by [33] and [34]. Radiometric observations were made at an incidence angle of 50º to the

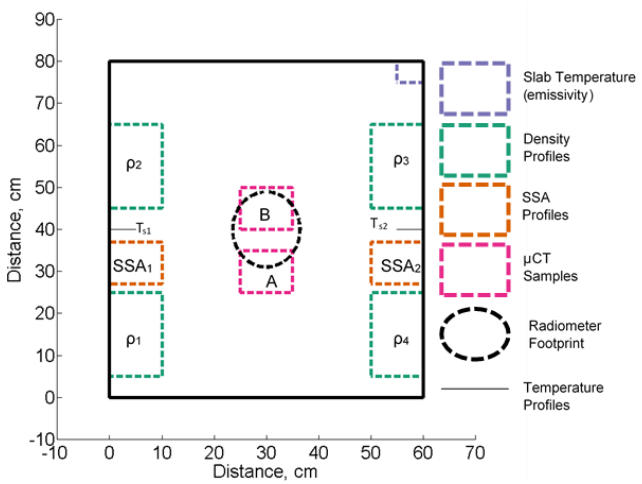

Fig 1: Approximate locations of the radiometric, macro- and microstructure observations of the ASMEx snow slabs. Individual µCT subsample locations are also shown. Adapted from [31] and [32].

vertical at 18.7-, 21.0-, 36.5-, 89.0-, and 150.0 GHz, at both horizontal (H-Pol) and vertical (V-Pol) polarizations. The reflective metal plate and the absorptive blackbody base were both allowed to acclimatise to the ambient physical air temperature of the snow, prior to the radiometric observations, to reduce the risk of the snow melting and re-freezing to the bases during the observations ([32]). Observations of the downwelling sky radiation at all available frequencies and at both polarizations were made immediately after the radiometric observations of the snow slabs, in order to observe any changes in -environmental downwelling radiation. Upon the completion of all radiometric observations, the physical properties of the snow were characterised using conventional snowpit observation techniques (as described by [18]) as well as by X-ray computer tomography (µCT, [29], [30]). This allowed for both conventional and modern observation techniques (in the case of microstructure parameterisation, subjective and objective observation techniques, respectively) to be used. Fig. 1 shows the approximate location of all physical observations made across the ASMEx slabs, as well as the calculated location of the radiometric footprint. Prior to the ASMEx campaign, iterative measurements of a reflective metal sheet upon the absorbing blackbody material were completed, in order to empirically find the dimensions of the radiometer footprint and the effects and positions of the associated side lobes. The centre of the Styrofoam positioner was very sensitive to the metallic strip, whilst the edges of the Styrofoam were hardly/not sensitive to the metallic strip, thus highlighting the location of the footprint.

This field of view characterisation was drawn upon a 'Styrofoam positioner' used throughout the ASMEx campaign (Figure 3.5 of [32]) to allow for numerous snow slabs to be observed from the same location, and thus keeping the radiometric footprint within the snow slabs. This could produce a potential source of error, as misalignment of the snow slabs with the positioner markings could result in different parts of the snow slab, or even the plastic support box, being present in the field of view. A second potential source of error is present, due to the fact that the snow slabs were not in the far field of the radiometers, due to the practicalities of the ASMEx campaign; however determining the impact of this error could

not be calculated without careful analysis, which is beyond the scope of this study.

III. Flux Coefficient Model

A. Deriving Slab Reflectivities and Transmissivities

The ASMEx observations were designed to measure the absorption and scattering properties of the extracted snow slabs. This was done by calculating the emissivity, reflectivity, and transmissivity of the extracted snow slabs using the observed microwave brightness temperatures of snow slabs upon the reflective metal base (T_{BM}) and upon the absorptive blackbody base (T_{BA}), as well as the snow slabs physical temperature (T_{phys}) and the downwelling sky radiation (T_{BSKY}). In order to calculate the absorption and scattering properties of the snow slabs, a Flux Coefficients Model based on a six-directional sandwich model, first detailed by [33], was used.

T_{BM} and T_{BA} are comprised from two individual sources; from the emission by the snow slab itself (governed by its physical temperature T_{phys}), and from the downwelling sky radiation reflected by the snow slab and base (where the total reflectivity are r_{met} and r_{abs} respectively). T_{BM}, therefore, is equal to:

$$T_{BM} = (1 - r_{met})T_{phys} + r_{met}T_{BSKY} \quad (2)$$

While T_{BA} is equal to:

$$T_{BA} = (1 - r_{abs})T_{phys} + r_{abs}T_{BSKY} \quad (3)$$

The total reflectivity of the snow upon the reflective metal plate and absorptive blackbody base (accounting for coherent wave interactions within the slab) are related to the internal reflectivities (r) and transmissivities (t), as well as the Fresnel reflectivities (r_i); expressed as:

$$r_{met} = r_i + (1 - r_i)^2 R_{met} \quad (4)$$

$$r_{abs} = r_i + (1 - r_i)^2 R_{abs} \quad (5)$$

where R_{met} and R_{abs} are functions of r, t, and r_i:

$$R_{met} = \frac{r + t^2(1-r)^{-1}}{1 - rr_i - r_i t^2(1-r)^{-1}} \quad (6)$$

$$R_{abs} = \frac{r + r_i t^2(1-rr_i)^{-1}}{1 - rr_i - (r_i t)^2(1-rr_i)^{-1}} \quad (7)$$

Figure 2 shows a schematic of the snow slab upon the base (either blackbody absorbing or the metal reflective base). The internal reflectivities, internal reflectivies, Fresnel reflectivies, and total reflectivity of the slab upon the different bases are shown for clarity.

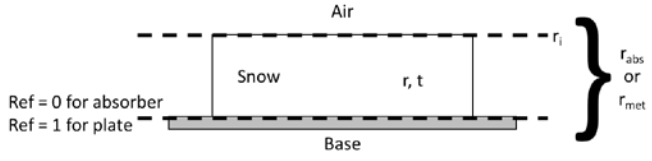

Fig 2: Schematic of the snow slab upon a material base (either a blackbody absorber or reflective metal base, detailing the numerous distinctive reflectivies used in Eqns. (4) – (7).

R_{met} and R_{abs} can be calculated from evaluated values of r_{abs} and r_{met} respectively (using (2) and (3)), if the value of r_i is known. As the snow interface was considered to be smooth, r_i was assumed to be equal to that of the Fresnel reflectivity. The Fresnel reflectivity was determined from the incidence angle and complex dielectric constant ε (where ε = ε' + iε'').

By solving (6) and (7), r and t of the individual slabs can be obtained. Rearranging (6) and (7) gives a pair of non-linear equations for the internal reflectivity and transmissivity of the slabs:

$$r = R_{abs}(1 - rr_i - (r_i t)^2(1 - rr_i)^{-1}) - r_i t^2(1 - rr_i) \quad (8)$$

$$t^2 = R_{met}\left((1 - rr_i)(1 - r) - r_i t^2\right) - r(1 - r) \quad (9)$$

where the values of R_{abs}, R_{met}, and r_{i} are known. [33] proposed an iterative solution to (8) and (9), by setting $r_i = 0$ for the first iteration:

$$r = R_{abs};\ t^2 = (R_{met} - R_{abs})(1 - R_{abs}) \quad (10)$$

This gave a first iterative solution for (8) and (9). Inserting the first iterative solution back into the pair of non-linear equations, with the calculated value of r_{i} gave a second iterative solution. This process was repeated until the old and new values varied by less than 0.0005.

B. Deriving Absorptive and Scattering Properties of Slabs

To link r and t to the absorption and scattering properties of the snow slabs, the six-directional Flux Coefficient Model, developed by [33] and used by [34], was applied. The six-directional Flux Coefficient Model accounts for the radiation propagating through the snow slab along the three principle axes, for a given frequency and polarization. Radiation propagating in the four horizontal directions represent the internally trapped radiation; whose internal incidence angle θ is greater than the critical angle θ_c:

$$\theta > \theta_c = arcsin\left(\frac{1}{\sqrt{\varepsilon'}}\right) \quad (11)$$

The vertical fluxes depict those that were not subject to total internal reflection. For isotropic and plane-parallel snow slabs, the six-flux model is transformed into a traditional two-flux model, where two-flux absorption (γ_a') and scattering (γ_b') coefficients are written in terms of the six-flux parameters:

$$\gamma_a' = \gamma_a(1 + 4\gamma_c(\gamma_a + 2\gamma_c)^{-1}) \quad (12)$$

$$\gamma_b' = \gamma_b + 4{\gamma_c}^2(\gamma_a + 2\gamma_c)^{-1} \quad (13)$$

where γ_a is the six-flux absorption coefficient, γ_b is the six-flux back scattering coefficient, and γ_c is the six-flux scattering coefficient around 90° (perpendicular to the direction of travel). [33] stated that r and t of a snow slab with thickness d could be calculated via:

$$r = r_0(1 - {t_0}^2)(1 - {r_0}^2{t_0}^2)^{-1} \quad (14)$$

$$t = t_0(1 - {r_0}^2)(1 - {r_0}^2{t_0}^2)^{-1} \quad (15)$$

where the one way transmissivity through the slab, t_0, is calculated via:

$$t_0 = exp\left(\frac{-\gamma d}{cos\theta}\right) \quad (16)$$

and where the reflectivity of infinite slab thickness, r_0 is calculated via:

$$r_0 = \gamma_b'(\gamma_a' + \gamma_b' + \gamma)^{-1} \quad (17)$$

Both r_0 and t_0 are calculated through a function of γ_a', γ_b', and the dampening coefficient γ,

$$\gamma = \sqrt{\gamma_a'(\gamma_a' + 2\gamma_b')} \quad (18)$$

[33] used a number of iterative processes to calculate the values of r_0 and t_0, in order to calculate the two-flux absorption and scattering coefficients, initially from values of R_{met} and R_{abs}.

In order to link the calculated values of r and t to those of r_0 and t_0, and thus to the six-flux coefficients, a second iterative process was used. (14) and (15) were rearranged to form another set of non-linear equations:

$$r_0 = \frac{-1+\sqrt{1+4G^2}}{2G}; G \equiv \frac{r_0}{1-{r_0}^2} = \frac{r}{t}\frac{t_0}{1-{t_0}^2} \quad (19)$$

$$t_0 = t(1 + {r_0}^2(1 - {t_0}^2)(1 - {r_0}^2)^{-1}) \quad (20)$$

Setting $t_0 = t$ allowed for a first iterative solution to be found for r_0 and t_0. Similar to the first iterative process, the iterative solutions were fed into the non-linear equations repeatedly, until the old and new values converged to within 0.0005. The values of γ_a' and γ_b' were calculated using rearranged forms of (17) and (18):

$$\gamma_a' = \gamma\frac{1-r_0}{1+r_0} \quad (21)$$

$$\gamma_b' = (\gamma + \gamma_a')\frac{r_0}{1-r_0} \quad (22)$$

where γ was calculated using (16). For isotropic scattering by snow crystals, the total six-flux scattering coefficient, γ_s is given by:

$$\gamma_s = 2\gamma_b + 4\gamma_c \quad (23)$$

and the ratio between γ_b and γ_c is given by:

$$\frac{2\gamma_c}{\gamma_b} = \frac{x}{1-x} \quad (24)$$

where

$$x = \sqrt{\frac{\varepsilon\prime-1}{\varepsilon\prime}} \quad (25)$$

The full set of six-flux coefficients (γ_a, γ_b, γ_c, and γ_s) can now be calculated from the values of the two-flux coefficients (using (12) and (13)), the complex dielectric constant of the snow slabs, and (21) - (25). By solving (2) to (25), using the ASMEx radiometer data and μCT observed bulk slab data, the ASMEx six-flux absorption and scattering coefficients were calculated.

The impact of the snow slabs not being in the far field is difficult to assess without careful analysis, which was beyond the scope of this study. Many parts of the six-flux model (such as total internal reflection) assumes planar waves, which is not entirely valid, and thus may introduce some discrepancies. For this study, these discrepancies have been neglected.

IV. Semi-Empirical Extinction Coefficient Calculation

The ASMEx radiometric, bulk physical characteristics and μCT bulk microstructure slab data was used with the Flux Coefficient Model described in Section III, to produce values of γ_a and γ_s, for each individual ASMEx slab. Fig. 3 shows a comparison of all calculated γ_a values with the equivalent absorption coefficient, calculated using the n-HUT model ($k_{a,HUT}$, (26)):

$$k_{a,HUT} = \left(4\pi(F\text{x}10^9)\right)\left(\sqrt{\mu_0\varepsilon_0\varepsilon'_{snow}}\right)\left(\sqrt{0.5\left(\sqrt{1+\left(\frac{\varepsilon''_{snow}}{\varepsilon'_{snow}}\right)^2}\right)-1}\right) \quad (26)$$

where F is frequency (GHz), μ_0 is the permeability of free space (4π x 10^{-7} H·m-1) , ε_0 is the permittivity of free space

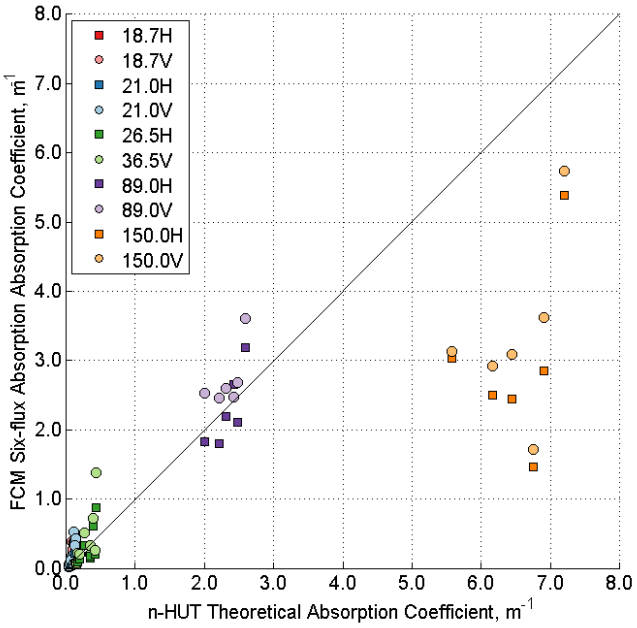

Fig 3: A comparison of retrieved absorption coefficient γ_a and the n-HUT theoretical absorption coefficient $k_{a,HUT}$ at 18.7- (red), 21.0- (blue), 36.5- (green), 89.0- (purple) and 150.0 (orange) GHz, at both horizontal (square, bold) and vertical (circle, pale) polarizations.

(8.85 x 10^{-12} F·m-1), and ε'_{snow} and ε''_{snow} are the real and imaginary dielectric constants of dry snow respectively. ε'_{snow} and ε''_{snow} are calculated internally within the n-HUT model, using formulae given in [15] and [35], with the latter using a Polder-van Santen mixing model.

All γ_a and $k_{a,HUT}$ values were calculated at all available frequencies, at both H-Pol and V-Pol, for each ASMEx slab. It is clear that, for the lower four frequencies, the values of γ_a are similar to that of the equivalent $k_{a,HUT}$ values, whilst at 150.0 GHz, the values of γ_a underestimate the equivalent $k_{a,HUT}$ values. The coefficient of determination, R^2, value of the γ_a values using the lower four frequencies at V-Pol is 0.945, whilst the R^2 value using all V-Pol γ_a is lower (0.765). This suggests that the Flux Coefficient Model has issues retrieving flux coefficients at 150.0 GHz. This is due to the extinction processes being dominated by surface processes. The small penetration depth at 150 GHz results in the emitted microwave radiation from the blackbody base or the reflected microwave radiation from the reflecting base being effectively scattered by the snow, before the radiation leaves the snowpack from the surface. Thus, due to the small penetration depth at 150.0 GHz, the presented methodology could not be applied at 150.0 GHz.

The closeness of the retrieved γ_a values to the $k_{a,HUT}$ values in the lower four frequencies (Fig. 3) suggest that the flux coefficient model retrieves accurately the absorption coefficients. For the ease of implementation within the n-HUT model, the absorption coefficient term of the new extinction coefficient was equal to that of the theoretical absorption coefficient already used by the n-HUT model.

The retrieved V-Pol six-flux scattering coefficients, calculated from the ASMEx slabs, were used to form the scattering coefficient term of the newly derived extinction coefficient. The horizontal polarization was seen to be more readily effected by layer and discontinuities within the snowpack, and was thus not used in the scattering coefficient calculation. The scattering coefficient term, using the optical diameter observations, was hypothesised to be in the form:

$$\gamma_s = \alpha(D_0)^{c_1}(F)^{c_2} \quad (27)$$

where c_1 and c_2 are the exponents of the optical diameter and frequency respectively, and α is a multiplication factor. To calculate the value of c_2, α and the optical diameter dependency can be combined to make $\beta = \alpha(D_0)^{c1}$. As the value of β is independent to the value of c_2, the values of β were normalised, in order to determine the value of c_2. Fig. 4 shows plotted

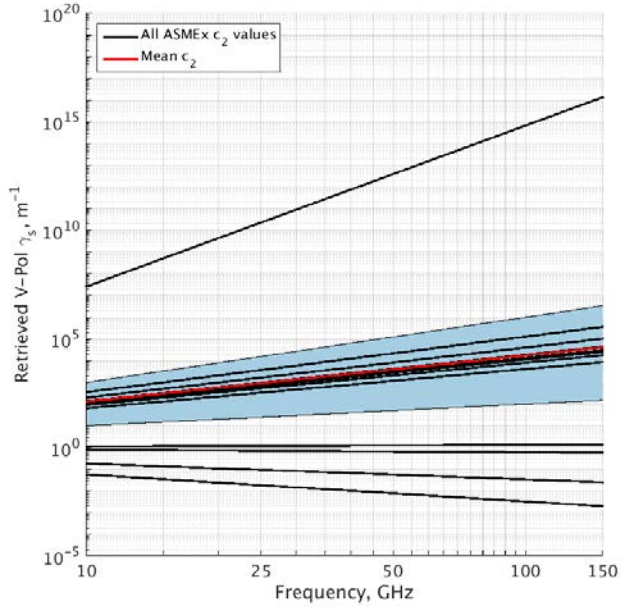

Fig 4: Frequency regression lines of retrieved V-Pol scattering coefficients γ_s for all ASMEx snow slabs. Regression lines were calculated and plotted in the form $\gamma_s = \beta(F)^{c1}$. The area shaded in blue denotes the threshold region, whilst the regression line plotted in read shows the mean c_2 value.

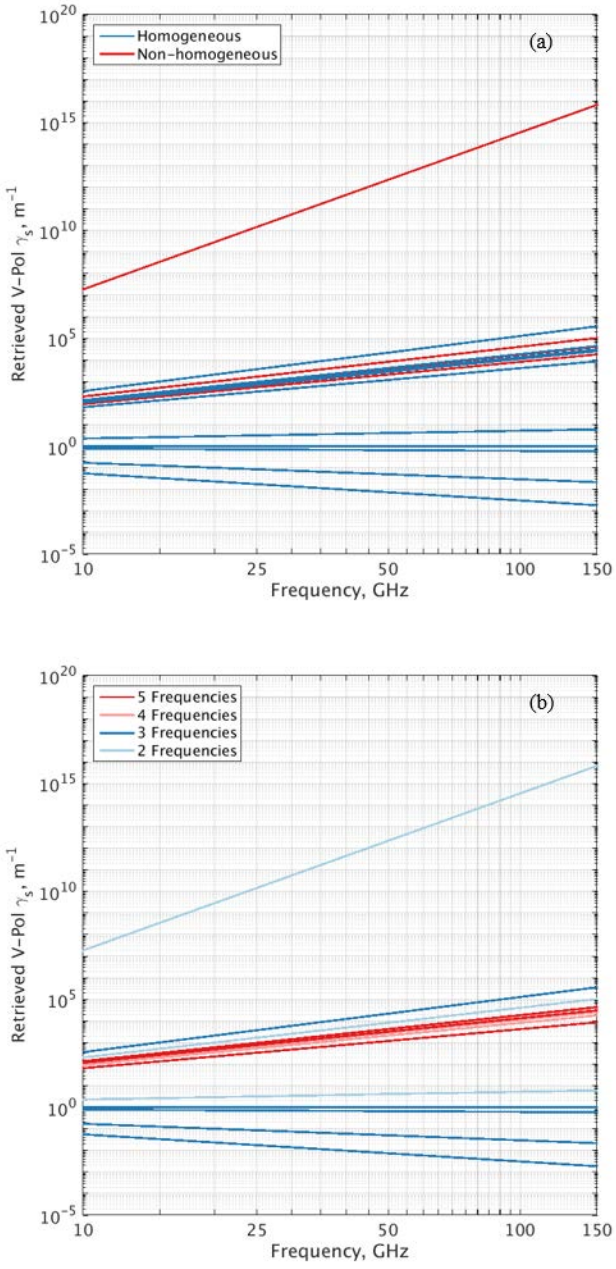

Fig 5: ASMEx γs frequency regression lines, denoting (a) homogeneous (blue) and non-homogeneous (red) slabs, using μCT properties to denote homogeneity, and (b) the number of frequency observations used to calculate the regression lines; 5 (dark red), 4 (light red), 3 (dark blue), and 2 (light blue).

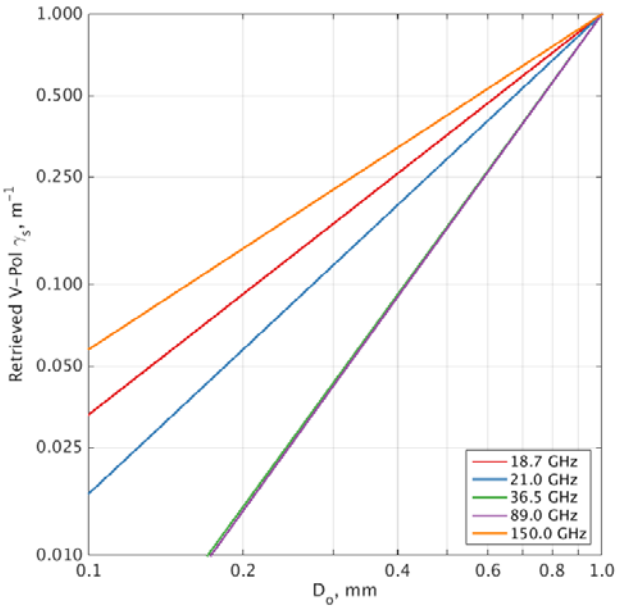

Fig 6: Optical diameter D_o regression lines of V-Pol γ_s for all frequencies used during ASMEx. Regression lines were calculated and plotted in the form $\Phi = \alpha(F)^{c2}$. Frequencies shown are 18.7- (red), 21.0- (blue), 36.5- (green), 89.0- (purple), and 150.0 (orange) GHz.

regression lines using V-Pol γ_s ASMEx values, in the form detailed by (27), setting $\beta = 1$.

After normalising the ASMEx V-Pol γ_s regression lines, a common band of frequency exponents were visible, in the range $1.81 < c_2 < 2.55$. Fig. 5 indicates that this common band of frequency exponents are due to the number of frequency observations made, and not the homogeneity of the slabs. The µCT profiles of D_o of each individual slab were assessed, and the standard deviation of each D_o profile was calculated. If the standard deviation of each D_o profile was below a threshold value of 0.15 mm, the slab was characterised as homogeneous. This standard deviation threshold was used for each slab with the exception of slab A03, which was deemed as "wet" ([31], [32]) and subsequently characterised as non-homogeneous. The regression laws shown in Fig. 4 were calculated using the bulk value of D_o, calculated from SSA values observed using the µCT analysis. To calculate a mean value of c_2 from the common band of frequency exponents, a threshold region of $1 < c_2 < 3$ was chosen, highlighted in blue in Fig. 4. The mean c_2 value within the threshold region was calculated to be 2.12, highlighted in red in Fig. 4.

The value of c_1 was calculated in a similar fashion to that of c_2; by rearranging (27) such that α and the frequency dependency were combined to make $\Phi = \alpha(F)^{c2}$, and then normalising the resulting expression, as Φ is independent of c_1. Fig. 5 shows the optical diameter regression laws (using $\Phi = 1$), using the V-Pol γ_s ASMEx values, at each of the five observed frequencies.

Unlike with the frequency regression laws, a common optical diameter exponent band is not present within Fig. 5, due to the small selection of individual frequencies. Analysis of the slab homogeneity and number of observations (similar to that of the frequency regression laws in Fig. 5) did not offer a clear

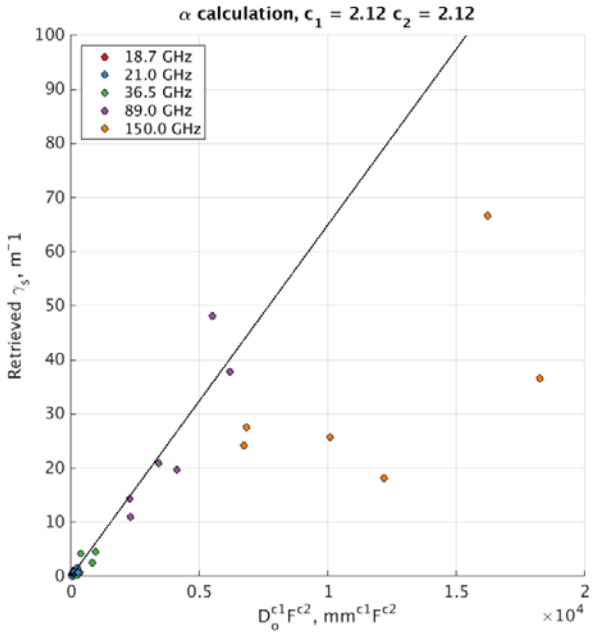

Fig 7: Regression line comparing the retrieved values of scattering coefficient γ_s against calculated values of $(D_o)^{c1}(F)^{c2}$ at 18.7- (red), 21.0- (blue), 36.5- (green), 89.0- (purple), and 150.0 (orange) GHz. The gradient on the plotted regression law denotes the value of α (0.0065 m^{-1}·mm$^{-2.12}$·GHz$^{-2.12}$).

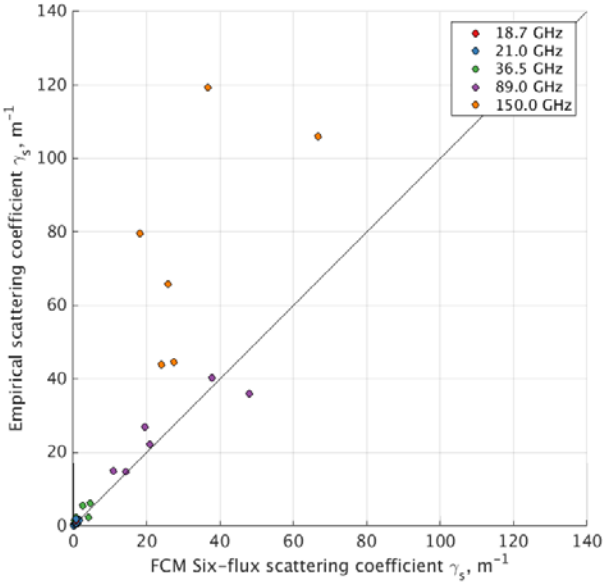

Fig 8: Comparison of retrieved values of scattering coefficient γ_s using the Flux Coefficient Model as detailed in [33] with values of γ_s calculated using (28), at 18.7- (red), 21.0- (blue), 36.5- (green), 89.0- (purple), and 150.0 (orange GHz), at vertical polarization. R^2 was calculated to be 0.637 across all five frequencies used, and 0.933 for the range 18.7 – 89.0 GHz.

indication regarding a common optical diameter exponent band. The 150.0 GHz regression law was not used in the calculation of the optical diameter exponent c_1, as the extinction properties at this frequency were dominated by surface processes due to the limiting penetration depth (as shown by the absorption coefficient retrieval in Fig. 3). Therefore, a mean value of c1 was determined for the regression laws of 18.7 -- 89.0 GHz, giving c_1 to be 2.12.

After the calculation of both c_1 and c_2, the value of α was determined by plotting all retrieved values of γ_s against calculated values of $(D_o)^{c1}(F)^{c2}$. A regression law was then calculated, setting the regression law intercept to the origin (as scattering tends to zero as snow crystal diameter decreases). Fig. 7 shows the retrieved γ_s values against calculated values of $(D_o)^{c1}(F)^{c2}$, as well as the resulting regression law; whose gradient, and thus α, is 0.0065 $m^{-1}\cdot mm^{-2.12}\cdot GHz^{-2.12}$.

After the calculation of α, c_1, and c_2, the exponents and multiplication factor were substituted into (27), in order to form an empirical scattering coefficient. Fig. 8 shows a comparison of the retrieved six-flux scattering coefficient, using the Flux Coefficient Model, with the empirical scattering coefficient model (calculated with (27)). It can be seen that for the lower four ASMEx frequencies, the empirical scattering coefficient accurately calculates the scattering coefficient, with a calculated R^2 value of 0.933 for the calculations in the range 18.7 -- 89.0 GHz. The calculations at 150.0 GHz, however, produce a large overestimation of scattering coefficient; a fact that can be seen as the calculated value of R^2 for all points is lower (0.637) than that of just the lower four frequencies (0.933). The empirical scattering coefficient calculated above can be implemented into the n-HUT model, using the pre-existing theoretical absorption coefficient, in order to produce a semi-empirical extinction coefficient:

$$k_e = \left(4\pi(F\text{x}10^9)\right)\left(\sqrt{\mu_0\varepsilon_0\varepsilon'_{snow}}\right)\left(\sqrt{0.5\left(\sqrt{1+\left(\frac{\varepsilon''_{snow}}{\varepsilon'_{snow}}\right)^2}\right)-1}\right)+ 0.0065(D_o)^{2.12}(F)^{2.12} \quad (28)$$

V. Evaluation of Semi-Empirical Coefficient with Sodankylä Radiometer Experiment

As an intermediate step to test the new extinction coefficient, n-HUT was used to simulate the brightness temperature of the snow slabs over the metal plate and over the absorber. Two sets of simulations were performed: firstly with the original extinction coefficient model given traditional (subjective) grain size observations, and secondly the new extinction coefficient model given in this paper and driven by optical grain diameter derived from micro-CT observations. Identical cutter densities were used in both sets of simulations. The changes in RMSE and bias (equations 29 and 30) from the original extinction coefficient to the new are shown in Table I.

TABLE I
Change in RMSE and BIAS for ASMEx Slabs

Frequency	RMSE (K)	Bias (K)
18.7	0.26	-0.65
21.0	0.21	-0.97
36.5	0.03	-8.23
89	-21.59	-36.89

In order to evaluate the n-HUT model with independent observations of a full snowpack, simulated brightness temperatures (using both the original and the new extinction coefficients) were compared to observed brightness temperatures, using data collected as part of the Sodankylä Radiometer Experiment (SoRaX). SoRaX consisted of numerous radiometric and snow property observations of the multiple layered snowpack within the Intensive Observation Area (IOA) at the Finnish Meteorological Institute Arctic Research Centre (FMI ARC). Radiometric observations at 18.7-, 21.0-, and 36.5 GHz were made, at a range of azimuth and elevation angles (Fig. 9). Radiometers were calibrated prior to the observations using both an ambient temperature calibration observations were aligned with the nearest profiles. Table II shows the radiometric azimuth and elevation angles corresponding to each SoRaX snow trench used. Profiles at 0 m and 5 m for the -50º elevation angle snow trench were not utilized in this analysis, as the centre of radiometric footprints were not deemed to be close enough to the SoRaX snowpits. Snow microstructure profiles within the -40º and -50º elevation angle snow trenches were chosen for simulation with the n-HUT model. The following observations of snow microstructure were made in each trench: a trench-long Near-

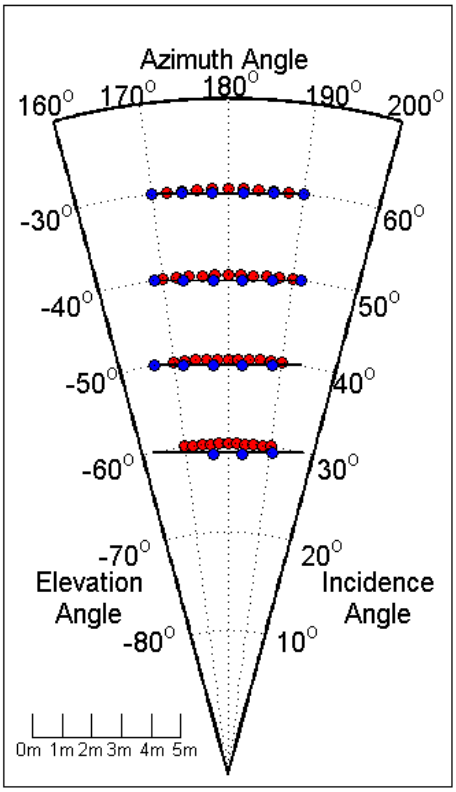

Fig 9: Azimuth and elevation angles of all radiometric (red) and snowpit (blue) observations in the SoRaX snow characterization campaign. The snowpit observations were spaced 1 m apart. The horizontal black line denotes the location of snow trenches and Near-Infrared photographs. Equivalent incidence angles are also shown alongside the corresponding elevation angle.

TABLE II
Azimuth angles associated with snowpit observations made across -40º and -50º elevation angles of the SoRaX campaign

Ele.	0 m	1 m	2 m	3 m	4 m	5 m
-40º	190	186	182	178	174	170
-50º	N/A	188	182	178	172	N/A

TABLE III
SoRaX SNOWPIT AND SNOW TRENCH OBSERVATIONS

Ele.	Obs	0 m	1 m	2 m	3 m	4 m	5 m
	NIR	X	X	X	X	X	X
	T_s	X	X			X	X
	ρ	X	X	X	X	X	X
-40º	*SSA*	X	X		X	X	X
	E				X		
	HS	X	X	X	X	X	X
	L	X	X			X	X
	NIR	X	X	X	X	X	X
	T_s			X	X		
	ρ	X	X	X	X	X	
-50º	*SSA*	X	X	X	X	X	X
	E				X		
	HS	X	X	X	X	X	X
	L			X	X	X	

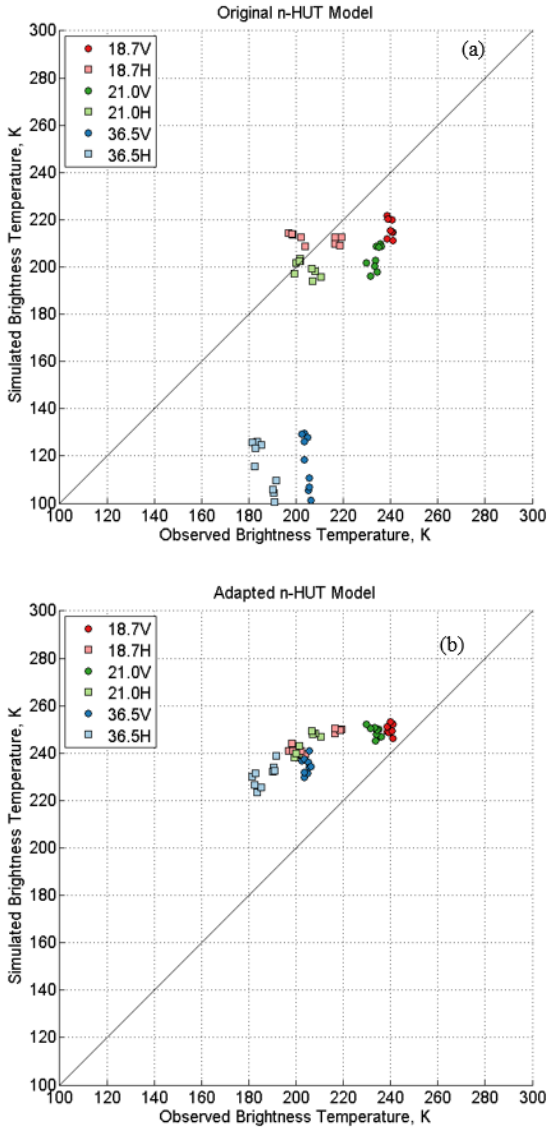

Fig 10: n-HUT model simulations using the extinction coefficient using (a) traditional grain size, and (b) Do derived from SSA observations, at 18.7- (red), 21.0- (green), and 36,5 (blue) GHz, at horizontal (square, pale) and vertical (circle, bold) polarizations.

Infrared photograph composite (NIR) for stratigraphic analysis ([36]), individual physical temperature (*Ts*) profiles, snow density (ρ_s) profiles using a 500 ml box cutter ([18] and [27]), Specific Surface Area (SSA) profiles using an IceCube instrument [24], [25]), grain size (*E*) profiles via macro photography analysis ([18]), layer thickness (*L*), and total snow height (*HS*) observations. Table III shows how measurement profiles were located in each trench. Where profiles did not have observations (e.g. physical temperature or visually determined traditional grain size) mean profiles were used from observations across the trench.

Snowpack stratigraphy in the -40º and -50º elevation trenches was input into the n-HUT model, using both the original extinction coefficient ([10], using visually determined grain size) and the semi-empirical extinction coefficient ((28), using optical diameter calculated from SSA observations), as a series of eight (-40º) or nine (-50º) homogeneous layers. Layers had a range of physical temperatures (-0.4ºC to -6.2ºC), densities (80 $kg \cdot m^{-3}$ to 322 $kg \cdot m^{-3}$), SSA (7.4 $m^2 \cdot kg^{-1}$ to 42.9 $m^2 \cdot kg^{-1}$), and grain size (0.25 mm to 3.0 mm). The underlying ground surface was characterised by its physical temperature (observed to be -0.83ºC by probe thermometers stationed across the IOA), as well as the permittivity of the ground, assumed to be 6 - 1j, ([11]).

Fig. 10 shows a comparison of the SoRaX observed brightness temperatures with the simulations using the n-HUT model, utilizing the original extinction coefficient (Fig. 10a), and the newly derived extinction coefficient (Fig. 10b). SoRaX n-HUT simulations were produced at 18.7, 21.0, and 36.5 GHz, at both horizontal and vertical polarizations. Although the semi-empirical extinction coefficient was calculated using only the vertical polarization, the simulations were completed using both horizontal and vertical polarizations for completeness. The results here on will focus purely on the vertical polarization.

As the only difference between n-HUT models were the two extinction coefficient models, differences in simulated brightness temperatures were a direct result of the scattering coefficients; the theoretical absorption coefficient was equal for both n-HUT simulations. Differences in microstructure parameters (visual grain size for Fig. 10a, optical diameter derived from observations of SSA for Fig. 10b) affected the resulting scattering coefficient. Simulation RMSE (29) and bias (30) values were calculated for each frequency and polarization, and displayed in Tables IV and V respectively. Fig. 10a and 10b demonstrate improvements made to the accuracy of the n-HUT

TABLE IV
RMSE VALUES FOR THE SIMULATED BRIGHTNESS TEMPERATURES (K) OF THE SoRaX SNOWPITS, FROM BOTH THE ORIGINAL AND ADAPTED N-HUT MODELS

Extinction Coefficient	Reference [10]		Equation (28)	
Freq. (GHz)	H-Pol	V-Pol	H-Pol	V-Pol
18.7	11.30	23.46	37.54	10.87
21.0	7.75	30.15	39.68	15.60
36.5	72.68	88.16	44.09	30.40

TABLE V
BIAS VALUES FOR THE SIMULATED BRIGHTNESS TEMPERATURES (K) OF THE SORAX SNOWPITS, FROM BOTH THE ORIGINAL AND ADAPTED N-HUT MODELS

Extinction Coefficient	Reference [10]		Equation (28)	
Freq. (GHz)	H-Pol	V-Pol	H-Pol	V-Pol
18.7	4.08	-23.08	37.12	10.62
21.0	-4.56	-29.88	39.63	15.17
36.5	-71.47	-87.36	43.98	30.22

model, especially at 36.5 GHz, when using the new extinction coefficient (28).

$$RMSE = \sqrt{\frac{\sum_1^n (T_{B,sim} - T_{B,obs})^2}{n}} \quad (29)$$

$$Bias = \frac{\sum_1^n (T_{B,sim} - T_{B,obs})}{n} \quad (30)$$

Tables IV and V show calculated RMSE and bias values at all frequencies and polarizations for both the extinction coefficients used. Magnitudes of RMSE and bias values decrease at vertical polarizations when using the new semi-empirical extinction coefficient. An error reduction is also seen at horizontal polarization at 36.5 GHz, however as the semi-empirical extinction equation was derived using only vertical polarizations, no conclusions can be drawn.

Similar magnitudes of RMSE and bias values suggests that a large portion of the errors are due to a persistent bias present within the n-HUT model. This error is present regardless of the extinction coefficient used; a fact that is shown in the unbiased RMSE values ((31), Table VI). Unbiased RMSE values have been calculated by subtracting bias values from observations, and recalculating the RMSE values. Table VI shows a decrease in magnitude in unbiased RMSE values when using the new extinction coefficient. This improvement is highlighted at 36.5 GHz, where unbiased RMSE values decrease from 13.25 K (using the original extinction coefficient) at vertical polarizations to 3.29 K.

TABLE VI
UNBIASED RMSE VALUES FOR THE SIMULATED BRIGHTNESS TEMPERATURES (K) OF THE SORAX SNOWPITS, FROM BOTH THE ORIGINAL AND ADAPTED N-HUT MODELS.

Extinction Coefficient	Reference [10]		Equation (28)	
Freq. (GHz)	H-Pol	V-Pol	H-Pol	V-Pol
18.7	10.35	4.24	5.58	2.23
21.0	6.27	3.97	1.97	3.63
36.5	13.25	11.85	3.29	3.31

$$Unbiased\ RMSE = \sqrt{\frac{\sum_1^n (T_{B,sim} - T_{B,obs} - Bias)^2}{n}} \quad (31)$$

A default value of 6 – 1j ([11]) was used for soil permittivity throughout. Values taken from [37] were used to assess the sensitivity of the unbiased RMSE values to the soil. The default value for soil permittivity was replaced with 3.42 – 0.005j and 4.47 – 0.33j at 18.7- and 36.5 GHz respectively, and the simulations rerun. It was found that the unbiased RMSE values were insensitive to the change in soil permittivity, with a difference in unbiased RMSE values of +0.5 K at 18.7 GHz, and -0.1 K at 36.5 GHz, across both the original and adapted n-HUT model simulations at horizontal and vertical polarizations.

VI. DISCUSSION

The immediate implications of the utilization of the semi-empirical extinction coefficient are two-fold. First, the reduction of the simulation errors suggests that the accuracy of the n-HUT model is increased, allowing for improved simulations of microwave signatures of a multiple-layer snowpacks, however this reduction in simulated errors is slight, and can only be discussed in the vertical polarization.

Second, the inclusion of objectively-derived optical diameter as a viable input parameter into the n-HUT model facilitates the parameterisation of microstructure size to take place via objective observations with increased precision relative to conventional observer-based grain size estimation methods.

It should be noted that there are numerous errors surrounding the derivation and evaluation of the semi-empirical extinction coefficient shown in this paper. Using the six-flux coefficient model with the ASMEx slab data produced a polarization difference between the six-flux horizontal and vertical scattering coefficients. This polarization difference was also present in [33], where the model was originally produced. Similarly to [33], this study focused on the vertical polarization when deriving the empirical scattering coefficient. This could be the reason behind the decrease in the accuracy of the H-Pol brightness temperature simulations by the n-HUT model.

During the ASMEx campaign, only three of the 14 measured slabs used all five available frequencies (as detailed by [31], [32]). This meant that the number of frequency observations were not consistent throughout ASMEx. The effects of the inconsistent number of frequency observations are apparent during the calculation of c_2 in Fig. 4b. Measuring all slabs at all five frequencies would reduce the uncertainty caused by the differing number of observations at different frequencies, and would allow for the influence of homogeneity (Fig. 4a) to be more pronounced.

The six-flux method of deriving the scattering coefficient is somewhat inconsistent with the strongly forward scattering assumption within n-HUT. Despite this, the intermediate evaluation of the new extinction coefficient model showed improved RMSE and Bias in comparison with the original method determined via transmission experiments that are more physically compatible with the radiative transfer solution method in n-HUT. The improvement given by objective microstructure as an input into the n-HUT model (rather than the subjective traditional grain size measurement) more than compensates for the difference in treatment of fluxes, and further improvements may be obtained by revisiting the strongly forward scattering assumption within n-HUT. The improvements are small for the slabs, but this is to be expected

given the thinness of the slabs and therefore small amount of scattering material. The larger improvement in RMSE and Bias at 89.0 GHz can be accredited to the extended frequency range that the semi-empirical extinction coefficient model offers (18.7 – 89.0 GHz) over the original (18 – 60 GHz).

The SoRaX dataset was primarily used to demonstrate the improvement in the adapted n-HUT model. The surface roughness of the SoRaX dataset was estimated through the use of the NIR photography (primarily used to determine snowpack stratigraphy). Any errors and uncertainties within the soil roughness estimations could have resulted in the errors in simulated brightness temperature. In addition to this, the soil permittivity was assumed to be constant across all snow pits. Assuming that all snow pits exhibited the same soil permittivity may have introduced errors into the soil reflectivity ([38]), resulting in uncertainties in the simulated brightness temperatures. However, simulation tests showed that changing the permittivity value within realistic values for frozen soil had only a minimal effect on results.

Figure 10a displays a general underestimation of brightness temperatures at 36.5 GHz, corroborating results by [14], suggesting underestimation of brightness temperature using the original n-HUT model for deep snow (snow depth was already 1 m on average during the pit excavation of SoRaX). Use of the new formulation of extinction coefficient reduces these underestimations (Fig. 10b), leading to a slight overestimation of brightness temperature across all frequencies and polarizations. This suggests the new formulation may mitigate for the limitations of the one-flux formulation in the n-HUT model, which was perceived as the main source of underestimation by [14]. However, further studies including measurements of deeper snow would be needed to ascertain this. Moreover, [14] applied measurement of E as inputs into the n-HUT and MEMLS models, making it difficult to directly compare with results here.

A possible area of future work would be to improve upon the semi-empirical extinction coefficient presented here, through the use of an optical diameter scaling parameter, to better optimize the extinction coefficient, and to better model the level of scattering taking place. An additional area of future work would be to compare the adapted n-HUT model with other microwave snow emission models, such as the Microwave Emission Model of Layered Snowpacks (MEMLS, [39]), the Dense Media Radiative Theory model (DMRT, [40]), and the Snow Microwave Radiative Transfer model (SMRT, [41]), using the SoRaX dataset, to assess the differences across the models.

The improved parameterization of model extinction coefficient improves the overall model formulation, and increases the accuracy of the brightness temperature simulations for the data sets used. It is anticipated that, when coupled with energy and mass balance models that incorporate detailed microstructure parameters (such as D_0), improved simulations will be realized. The improvements also have implications for approaches that combine ground, airborne, or satellite-based observations, through data assimilation schemes, to better estimate global snow mass and SWE.

VII. Conclusion

Semi-empirical microwave emission models have been used in conjunction with passive microwave remote sensing data, in order to extract global snow mass and SWE from satellite data. This paper presents the derivation of a semi-empirical extinction coefficient model, for use with the n-HUT model, utilizing objective calculations of optical diameter instead of the traditionally used grain size E. The semi-empirical extinction coefficient model was derived using a six-flux coefficient model, using data collected as part of the ASMEx campaign. Both the original and the semi-empirical extinction coefficient were used with the n-HUT model to simulate the brightness temperature of a naturally evolved, multi-layer snowpack observed during the separate SoRaX campaign on the following year, at 18.7, 21.0, and 36.5 GHz. The results from this study show that using the semi-empirical coefficient model in conjunction with data collected from SoRaX produced more accurate simulations of the microwave signature of a multiple-layered snowpack at vertical polarizations than with the previous empirical formulation of the extinction coefficient, and produced lower unbiased RMSE values at both polarizations. Future work into the source of the polarization difference in retrieved scattering coefficient will ultimately lead to a further improvement to the accuracy of the semi-empirical extinction coefficient, and thus the simulated brightness temperatures from the n-HUT model at both polarizations. The data and methodologies applied here could potentially benefit the development and evaluation of other similar models as well.

VIII. Acknowledgements

We thank the staff of FMI Arctic Research Centre in Sodankylä for performing the ground-based radiometer measurements and macro- and microstructure measurements for both the ASMEx and the SoRaX campaigns. We also thank the staff of WSL Institute of Snow and Avalanche Research SLF for the SMP instrument and for the SMP and micro-CT analyses of the snow samples. The manuscript preparation was supported by the EU 7th Framework Program project “European–Russian Centre for cooperation in the Arctic and Sub-Arctic environmental and climate research” (EuRuCAS, Grant no. 295068). We thank two anonymous reviewers whose comments have helped improve this paper greatly.

References

[1] J. Cohen and D. Rind, “The Effect of Snow Cover on the Climate,” *J. Clim.*, vol. 4, pp. 689 – 706, 1991.

[2] T. Barnett, J. Adam, and D. Lettenmaier, “Potential impacts of a warming climate on water availability in snow-dominated regions.,” *Nature*, vol. 438, no. 7066, pp. 303–9, Nov. 2005.

[3] A. Chang, J. Foster, and D. Hall, “Nimbus-7 SMMR derived global snow cover parameters,” *Ann. Glaciol.*, vol. 9, pp. 39 – 44, 1987.

[4] J. Hollinger, J. Peirce, and G. Poe, “SSM/I Instrument Evaluation,” *IEEE Trans. Geosci. Remote Sens.*, vol. 28, no. 5, pp. 781 – 790, 1990.

[5] R. Kelly, A. Chang, L. Tsang, and J. Foster, “A Prototype AMSR-E Global Snow Area and Snow

Depth Algorithm," *IEEE Trans. Geosci. Remote Sens.*, vol. 41, no. 2, pp. 230 – 242, 2003.
[6] M. Takala, J. Pulliainen, S. Metsamaki, and J. Koskinen, "Detection of snowmelt using spaceborne microwave radiometer data in Eurasia from 1979 to 2007," *IEEE Trans. Geosci. Remote Sens.*, vol. 47, no. 9, pp. 2996–3007, 2009.
[7] J. Foster, D. Hall, and A. Chang, "Remote sensing of snow," *Eos, Trans. Am. Geophys. Union*, vol. 68, no. 32, p. 682, 1987.
[8] J. Foster, C. Sun, J. Walker, R. Kelly, A. Chang, J. Dong, and H. Powell, "Quantifying the uncertainty in passive microwave snow water equivalent observations," *Remote Sens. Environ.*, vol. 94, no. 2, pp. 187–203, 2005.
[9] A. Chang, R. Kelly, E. Josberger, R. Armstrong, J. Foster, and N. Mognard, "Analysis of Ground-Measured and Passive-Microwave-Derived Snow Depth Variations in Midwinter across the Northern Great Plains," *J. Hydrometeorol.*, vol. 6, pp. 20–33, 2005.
[10] M. Hallikainen, F. Ulaby, and T. Van Deventer, "Extinction Behavior of Dry Snow in the 18- to 90-GHz Range," *IEEE Trans. Geosci. Remote Sens.*, vol. GE-25, no. 6, pp. 737–745, 1987.
[11] J. Pulliainen, J. Grandell, and M. Hallikainen, "HUT snow emission model and its applicability to snow water equivalent retrieval," *IEEE Trans. Geosci. Remote Sens.*, vol. 37, no. 3, pp. 1378–1390, 1999.
[12] J. Lemmetyinen, J. Pulliainen, A. Rees, A. Kontu, Y. Qiu, and C. Derksen, "Multiple-layer adaptation of HUT snow emission model: Comparison with experimental data," *IEEE Trans. Geosci. Remote Sens.*, vol. 48, no. 7, pp. 2781–2794, 2010.
[13] F. Vachon, K. Goita, D. Seve, and A. Royer, "Inversion of a Snow Emission Model Calibrated With In Situ Data for Snow Water Equivalent Monitoring," *IEEE Trans. Geosci. Remote Sens.*, vol. 48, no. 1, pp. 59 – 71, 2010.
[14] J. Pan, M. Durand, M. Sandells, J. Lemmetyinen, E. Kim, J. Pulliainen, A. Kontu, and C. Derksen, "Differences between the HUT snow emission model and MEMLS and their effects on brightness temperature simulation," *IEEE Trans. Geosci. Remote Sens.*, vol. 54, no. 4, pp. 2001–2019, 2016.
[15] C. Mätzler, "Applications of the Interaction of Microwaves with the Natural Snow Cover," *Remote Sens. Rev.*, vol. 2, no. 2, pp. 259–387, 1987.
[16] C. Mätzler, "Microwave Properties of Ice and Snow," in *Solar System Ices: Based on Reviews Presented at the International Symposium "Solar System Ices" held in Toulouse, France, on March 27–30, 1995*, 1st ed., vol. 227, B. Schmitt, C. De Bergh, and M. Festou, Eds. Dordrecht: Springer Netherlands, 1998, pp. 241–257.
[17] C. Fierz, R. Armstrong, Y. Durand, P. Etchevers, E. Greene, D. McClung, K. Nishimura, P. Satyawali, and S. Sokratov, "The International Classification for Seasonal Snow on the Ground," in *IHP-VII Technical Documents in Hydrology*, 2009, pp. 1 – 80.
[18] L. Leppänen, A. Kontu, H.-R. Hannula, H. Sjöblom, and J. Pulliainen, "Sodankylä manual snow survey program," *Geosci. Instrumentation, Methods Data Syst.*, vol. 5, no. 1, pp. 163–179, May 2016.
[19] B. Montpetit, A. Royer, A. Langlois, M. Chum, P. Cliche, A. Roy, N. Champollion, G. Picard, F. Dominé, and R. Obbard, "In-situ Measurements for Snow Grain Size and Shape Characterization Using Optical Methods," in *68th Eastern Snow Conference*, 2011, pp. 173–188.
[20] L. Leppänen, A. Kontu, J. Vehviläinen, J. Lemmetyinen, and J. Pulliainen, "Comparison of traditional and optical grain-size field measurements with SNOWPACK simulations in a taiga snowpack," *J. Glaciol.*, vol. 61, no. 255, pp. 151–162, 2015.
[21] C. Carmagnola, S. Morin, Lafaysse M., F. Domine, B. Lesaffre, Y. Lejeune, G. Picard, and L. Arnaud, "Implementation and evaluation of prognostic representations of the optical diameter of snow in the SURFEX/ISBA-Crocus detailed snowpack model," *Cryosph.*, vol. 8, pp. 417–437, 2014.
[22] L. Legagneux, A. Cabanes, and F. Dominé, "Measurement of the specific surface area of 176 snow samples using methane adsorption at 77 K," *J. Geophys. Res.*, vol. 107, no. D17, p. 4335, 2002.
[23] B. Montpetit, A. Royer, A. Langlois, P. Cliche, A. Roy, N. Champollion, G. Picard, F. Domine, and R. Obbard, "Instruments and Methods New shortwave infrared albedo measurements for snow specific surface area retrieval," *J. Glaciol.*, vol. 58, no. 211, pp. 941 – 952, 2012.
[24] J. Gallet, F. Dominé, C. Zender, and G. Picard, "Measurement of the specific surface area of snow using infrared reflectance in an integrating sphere at 1310 and 1550 nm," *Cryosph.*, vol. 3, no. 2009, pp. 167–182, 2009.
[25] N. Zuanon, "IceCube, a portable and reliable instrument for snow specific surface area measurement in the field," in *International Snow Science Workshop Grenoble - Chamonix Mont-Blance*, 2013, pp. 1020–1023.
[26] M. Schneebeli, C. Pielmeier, and J. Johnson, "Measuring Snow Microstructure and Hardness using a High Resolution Penetrometer," *Cold Reg. Sci. Technol.*, vol. 30, no. 1, pp. 305–311, 1999.
[27] M. Proksch, N. Rutter, C. Fierz, and M. Schneebeli, "Intercomparison of snow density measurements: bias, precision, and vertical resolution," *Cryosph.*, vol. 10, pp. 371–384, 2016.
[28] M. Proksch, H. Löwe, and M. Schneebeli, "Density, specific surface area and correlation length of snow measured by high-resolution penetrometry," *J. Geophys. Res.-Earth Surf.*, vol. 120, no. 2, pp. 346–362, 2015.
[29] M. Schneebeli and S. Sokratov, "Tomography of temperature gradient metamorphism of snow and associated changes in heat conductivity," *Hydrol. Process.*, vol. 18, no. 18, pp. 3655–3665, 2004.
[30] M. Heggli, E. Frei, and M. Schneebeli, "Snow replica method for three-dimensional X-ray

microtomographic imaging," *J. Glaciol.*, vol. 55, no. 192, pp. 631–639, 2009.

[31] W. Maslanka, L. Leppänen, A. Kontu, M. Sandells, J. Lemmetyinen, M. Schneebeli, M. Proksch, M. Matzl, H.-R. Hannula, and R. Gurney, "Arctic Snow Microstructure Experiment for the development of snow emission modelling," *Geosci. Instrumentation, Methods Data Syst.*, vol. 5, pp. 85–94, 2016.

[32] W. Maslanka, "Extinction of Microwave Radiation in Snow," University of Reading, 2017.

[33] A. Wiesmann, C. Mätzler, and T. Weise, "Radiometric and Structral Measurements of Snow Samples," *Radio Sci.*, vol. 33, no. 2, pp. 273 – 289, 1998.

[34] A. Toure, K. Goïta, A. Royer, C. Mätzler, and M. Schneebeli, "Near-infrared digital photography to estimate snow correlation length for microwave emission modeling," *Appl. Opt.*, vol. 48, no. 36, pp. 6723–6733, 2008.

[35] M. Hallikainen, F. Ulaby, and M. Abdelrazik, "Dielectric Properties of Snow in the 3 to 37 GHz range," *IEEE Trans. Antennas Propag.*, vol. AP-34, no. 11, pp. 1329 – 1340, 1986.

[36] K. Tape, N. Rutter, H. Marshall, R. Essery, and M. Sturm, "Instruments and methods recording microscale variations in snowpack layering using near-infrared photography," *J. Glaciol.*, vol. 56, no. 195, pp. 75–80, Apr. 2010.

[37] B. Montpetit, A. Royer, A. Roy, and A. Langlois, "In-situ passive microwave emission model parameterization of sub-arctic frozen organic soils," *Remote Sens. Environ.*, vol. 205, no. January, pp. 112–118, 2018.

[38] A. Roy, G. Picard, A. Royer, B. Montpetit, F. Dupont, A. Langlois, C. Derksen, and N. Champollion, "Brightness temperature simulations of the Canadian seasonal snowpack driven by measurements of the snow specific surface area," *IEEE Trans. Geosci. Remote Sens.*, vol. 51, no. 9, 2013.

[39] A. Wiesmann and C. Mätzler, "Microwave Emission Model of Layered Snowpacks," *Remote Sens. Environ.*, vol. 70, no. 3, pp. 307–316, 1999.

[40] G. Picard, L. Brucker, A. Roy, F. Dupont, M. Fily, and A. Royer, "Simulation of the microwave emission of multi-layered snowpacks using the dense media radiative transfer theory: the DMRT-ML model," *Geosci. Model Dev.*, vol. 6, pp. 1061–1078, 2013.

[41] G. Picard, M. Sandells, and H. Löwe, "SMRT: an active-passive microwave radiative transfer model for snow with multiple microstructure and scattering formulations (v1.0)," *Geosci. Model Dev.*, vol. 11, pp. 2763–2788, 2018.